Supplementary Information (SI) for New Journal of Chemistry.

Fe single-atom catalysts embedded in reduced graphene oxide for electrochemical detection of uric acid and hydrogen peroxide

Jinxin Zuo[a], Xiaolong Chen[a], Chaowang Huang[a], Meina Guo[a], Qiao Hu[a], Jing Zhang[a], Mingdong Hu[ab,*], Peng Zhao[a,*]

[a] Department of Geriatrics and Special Services Medicine, Xinqiao Hospital of Army Medical University, Chongqing 400037, China

[b] Department of Health Management, Xinqiao Hospital of Army Medical University, Chongqing 400037, China

* E-mail addresses: humingdong@tmmu.edu.cn; zhaopeng@tmmu.edu.cn

S1. Materials and instruments

Indium tin oxide glass (SPE) was purchased from Rui Zhi Han Xing Technology Co., Ltd (Beijing, China). Zinc nitrate hexahydrate ($Zn(NO_3)_2 \cdot 6H_2O$) was purchased from Chuandong Chemical Industry Group (Chongqing, China). Dimethylimidazole (2-mIM), iron nitrate ($Fe(NO_3)_3 \cdot 9H_2O$), graphene oxide (GO), uric acid (UA), ascorbic acid (AA), dopamine hydrochloride (DA), glucose (Glu), urea (Ure), creatinine (Cre), etc. were obtained from Aladdin Biochemical Technology Co., Ltd. (Shanghai, China). Human Serum AB was purchased from NovoBiotechnology Co., Ltd. (Beijing, China).

The morphology was characterized by field-emission scanning electron microscope (SEM, Zeiss Gemini 360) and transmission electron microscopy (TEM, JEOL JEM-F200). The elemental compositions were clarified by X-ray photoelectron spectroscopy (XPS, Thermo Scientific-K-ALPHA). The atomic sites were determined by aberration-corrected high-angle annular dark-field scanning transmission electron microscopy (AC-HAADF-STEM, JEOL JEM-ARM200F). All electrochemical measurements were performed on a portable electrochemical analyzer (EmStat4R).

S2. Supplementary Figures

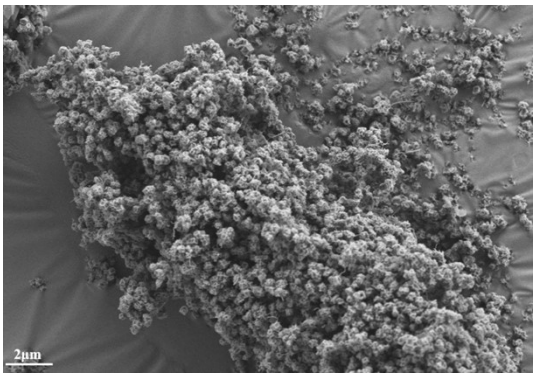

Fig. S1. SEM image of FeSACs.

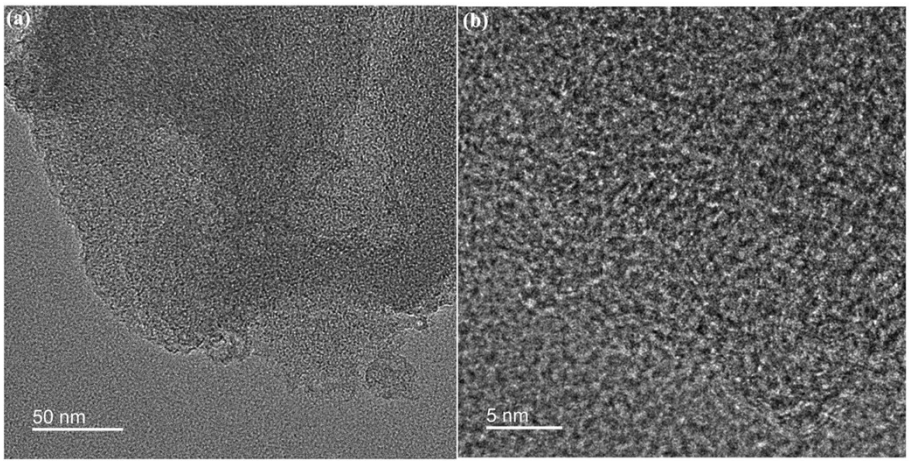

Fig. S2. High-resolution TEM images of FeSACs.

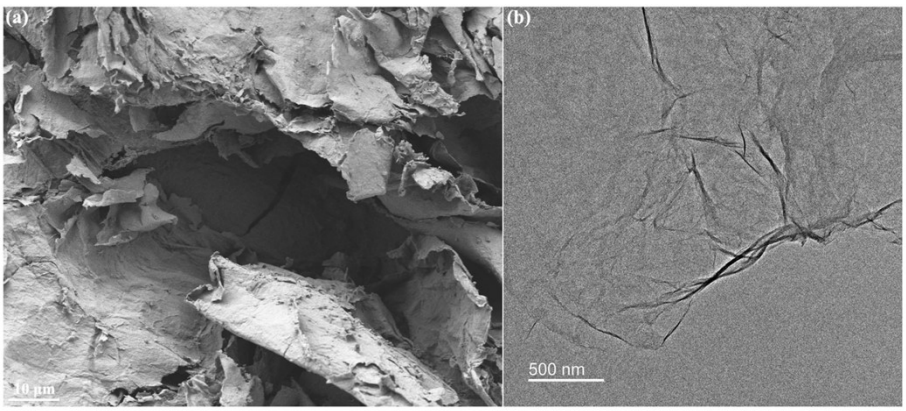

Fig. S3. SEM and TEM images of RGO.

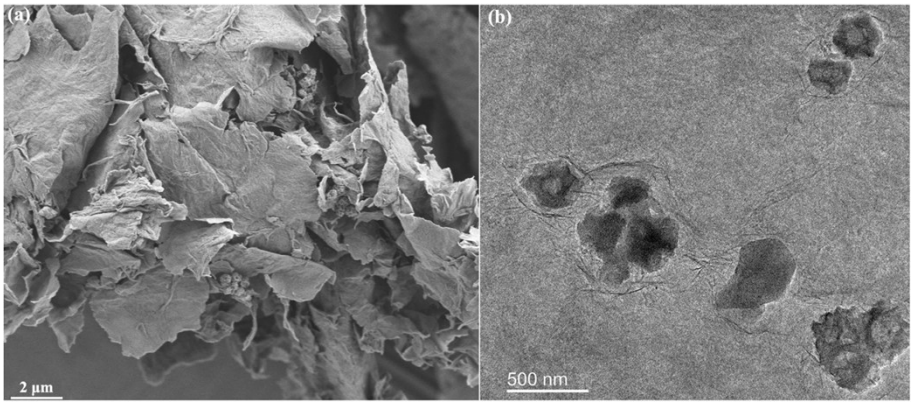

Fig. S4. SEM and TEM images of FeSACs@RGO.

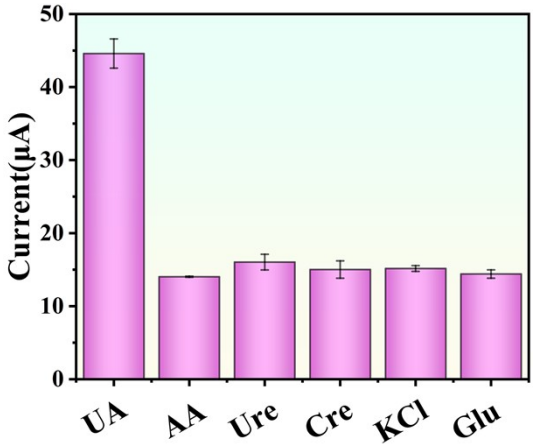

Fig. S5. Current of FeSACs@RGO/SPE toward 200 μM UA.

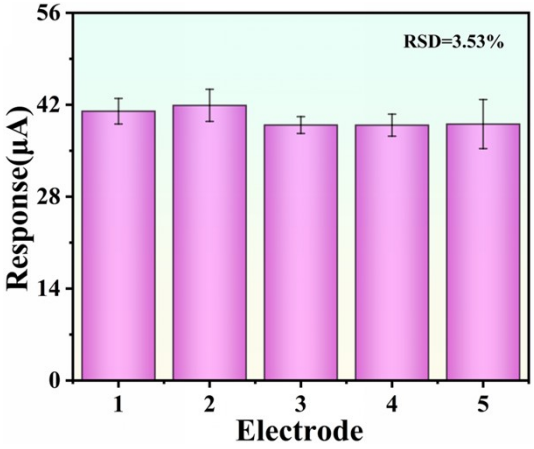

Fig. S6. Responses of five independent FeSACs@RGO/SPE toward 200 μM UA .

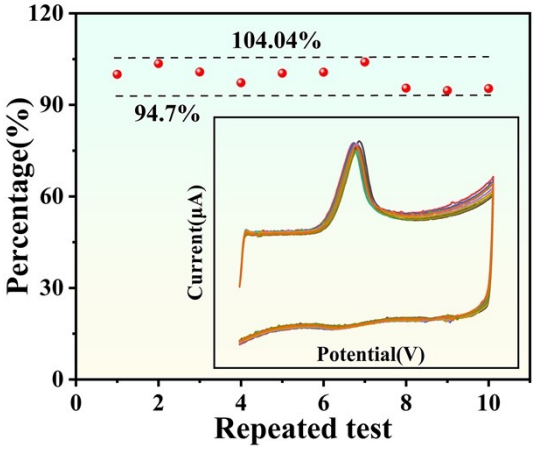

Fig. S7. Responses of FeSACs@RGO/SPE toward 200 μM UA during 10 repeated test.

The Fe-N coordination structure and the catalytic performance of FeSACs distinctly follows the principle of "structure-activity relationship". Specifically, the coordination structure could modulate the electronic structure of the Fe active sites (such as the d-band center position), which not only directly influences its electron transport capacity but also significantly regulates the adsorption strength for H_2O_2. The catalytic mechanism is illustrated in Fig. S8. The H_2O_2 molecule is initially adsorbed onto the single-metal atom in SAC. Then, the adsorbed H_2O_2 readily undergoes homolytic cleavage, producing two hydroxyl groups. One hydroxyl group desorbs, yielding a free hydroxyl radical. The remaining adsorbed hydroxyl reacts with a proton under acidic conditions, forming a H_2O molecule attached to the metal center. Finally, desorption of the H_2O molecule regenerates the catalyst to its original state.

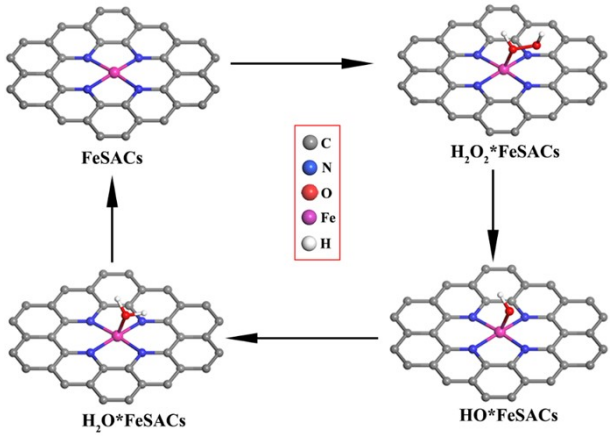

Fig. S8. Schematic illustration of the catalytic mechanism of H_2O_2 on FeSACs.

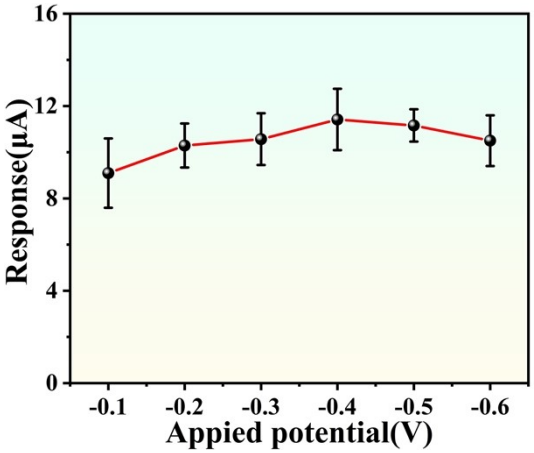

Fig. S9. The influence of applied potential on H_2O_2 response.

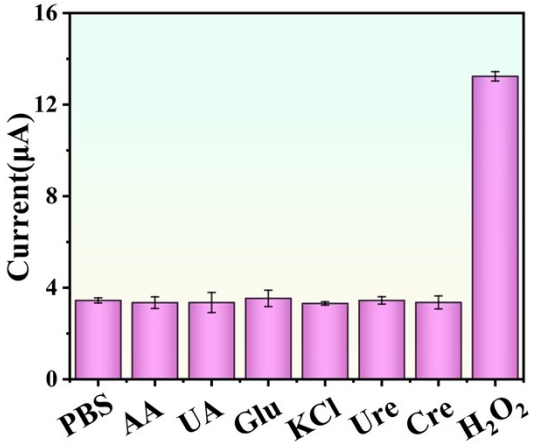

Fig. S10. Current responses of FeSACs@RGO/SPE toward different substances.

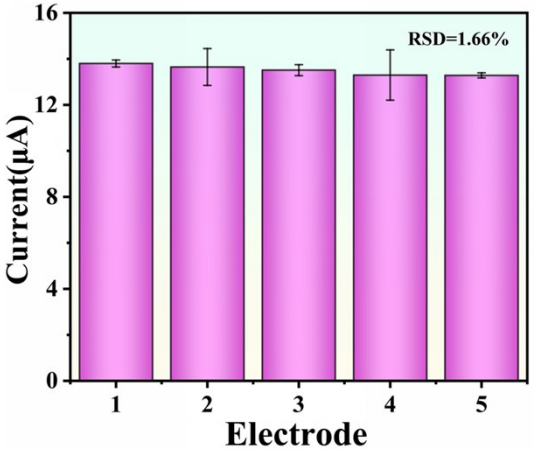

Fig. S11. Responses of five independent FeSACs@RGO/SPE toward 200 μM H_2O_2.

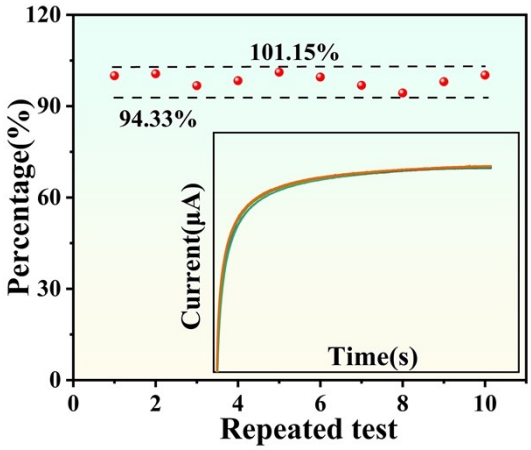

Fig. S12. Responses of FeSACs@RGO/SPE toward 200 μM H_2O_2 during 10 repeated test.

Table S1. Comparison of some recent electrochemical sensors for UA detection

Electrode material	Linear range (μM)	LOD (μM)	Ref.
FeNS/MWCNT	5-500	3.26	[1]
$CoNiFe_2O_4$	4-5280	6.38	[2]
PyTS@$Ti_3C_2T_x$	5-100	0.48	[3]
Ce-BTC@MoS_2	5-2500	5.00	[4]
MWCNT-COOH	0-1600	3.58	[5]
ENi-hMoS_2	100-9000	7.30	[6]
PTA/CeO_2@Pt	10-138	1.04	[7]
Co_3O_4 nanosheets	5-200	5.00	[8]
FeSACs@RGO	5-100	3.06	This work

Table S2. Comparison of some recent electrochemical sensors for H_2O_2 detection

Electrode material	Linear range (μM)	LOD (μM)	Ref.
CuO-CeO_2/MXene	5-100	1.67	[9]
FeCu-NZs	0.1-3800	0.06	[10]
Co@MOF-808	10-450	1.3	[11]
$NiCo_2O_4$-$Ti_3C_2T_x$	20-100	6	[12]
Pt1-rGO@PILs	2.3-250	1.5	[13]
FeSACs@RGO	5-4000	5.11	This work

Table S3. Results for UA detection in serum samples

Sample	Added (μM)	Found (μM)	Recovery (%)	RSD (%)
1	20	20.96	112.85	5.57
2	50	45.16	90.33	4.44
3	100	90.30	90.30	6.45

Table S4. Results for H_2O_2 detection in serum samples

Sample	Added (μM)	Found (μM)	Recovery (%)	RSD (%)
1	50	48.61	87.96	4.19
2	100	89.37	89.37	7.78
3	200	197.15	98.58	3.63

References

1. Joshi A et al, Multiwalled carbon nanotubes supported Fe nanostructured interfaces for electrochemical detection of uric acid. Microchem. J., 2024, 204, 110934. https://doi.org/10.1016/j.microc.2024.110934
2. John J F et al, Cobalt doped $NiFe_2O_4$ on 3D nickel foam substrate for electrochemical detection of uric acid. Surf, Interfaces, 2024, 44, 103629. https://doi.org/10.1016/j.surfin.2023.103629
3. Chen F et al, A Wearable Electrochemical Biosensor Utilizing Functionalized $Ti_3C_2T_x$ MXene for the Real-Time Monitoring of Uric Acid Metabolite. Anal. Chem., 2024, 96, 3914-3924. https://doi.org/10.1021/acs.analchem.3c05672
4. Zha X et al, Snowflake-like Ce-BTC@MoS_2 heterojunction for high-performance uric acid detection. Sens. Actuators B., 2025, 422, 136474. https://doi.org/10.1016/j.snb.2024.136474
5. Li Z et al, A Dual-Function Wearable Electrochemical Sensor for Uric Acid and Glucose Sensing in Sweat. Biosens., 2023, 13, 105. https://doi.org/10.3390/bios13010105
6. Rehman A et al, Perforated MoS_2 nanosheets adorned with Ni nanoparticles: An electrochemical sensor for concurrent detection of dopamine and uric acid. Microchem. J., 2025, 209, 112821. https://doi.org/10.1016/j.microc.2025.112821
7. Yu S et al, PTA/CeO_2@Pt-based electrochemical sensors to detect xanthine and uric acid, and evaluate fish freshness. Chem. Eng. J., 2024, 490, 151646. https://doi.org/10.1016/j.cej.2024.151646
8. Nagal V et al, Hexagonal cobalt oxide nanosheet-based enzymeless electrochemical uric acid sensor with improved sensitivity. New. J. Chem., 2023, 47, 4206-4212. https://doi.org/10.1039/d2nj06331j

9. Zhou K et al, A novel electrochemical sensor based on CuO-CeO_2/MXene nanocomposite for quantitative and continuous detection of H_2O_2. J. Electroanal. Chem., 2022, 921, 116655. https://doi.org/10.1016/j.jelechem.2022.116655
10. Gao H et al, Ultrasensitive detection of H_2O_2 via electrochemical sensor by graphene synergized with MOF-on-MOF nanozymes. Microchim. Acta, 2024, 191, 482. https://doi.org/10.1007/s00604-024-06541-8
11. Chang Y-S et al, Electrodeposition of pore-confined cobalt in metal-organic framework thin films toward electrochemical H_2O_2 detection. Electrochim. Acta, 2020, 347, 136276. https://doi.org/10.1016/j.electacta.2020.136276
12. Mohanapriya D et al, In situ developed $NiCo_2O_4$-$Ti_3C_2T_x$ nanohybrid towards non-enzymatic electrochemical detection of glucose and hydrogen peroxide. J. Mater. Chem. B., 2025, 13, 2306-2316. https://doi.org/10.1039/d4tb02265c
13. Shekh M I et al, Facile microwave-assisted synthesis of Pt single atom anchored on poly (ionic liquids) functionalized reduced graphene oxide for ultrasensitive detection of H_2O_2. J. Environ. Chem. Eng., 2023, 11, 110238. https://doi.org/10.1016/j.jece.2023.110238